






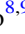





A NICER View of PSR J0030+0451: Evidence for a Global-scale Multipolar Magnetic Field

A. V. Bilous¹ , A. L. Watts¹ , A. K. Harding² , T. E. Riley¹ , Z. Arzoumanian³, S. Bogdanov⁴ , K. C. Gendreau³,
P. S. Ray⁵ , S. Guillot^{6,7} , W. C. G. Ho^{8,9} , and D. Chakrabarty¹⁰ 

¹ Anton Pannekoek Institute for Astronomy, University of Amsterdam, Science Park 904, 1090GE Amsterdam, The Netherlands; hanna.bilous@gmail.com

² Astrophysics Science Division, NASA Goddard Space Flight Center, Greenbelt, MD 20771, USA

³ X-Ray Astrophysics Laboratory, NASA Goddard Space Flight Center, Code 662, Greenbelt, MD 20771, USA

⁴ Columbia Astrophysics Laboratory, Columbia University, 550 West 120th Street, New York, NY 10027, USA

⁵ Space Science Division, U.S. Naval Research Laboratory, Washington, DC 20375, USA

⁶ IRAP, CNRS, 9 avenue du Colonel Roche, BP 44346, F-31028 Toulouse Cedex 4, France

⁷ Université de Toulouse, CNES, UPS-OMP, F-31028 Toulouse, France

⁸ Department of Physics and Astronomy, Haverford College, 370 Lancaster Avenue, Haverford, PA 19041, USA

⁹ Mathematical Sciences, Physics and Astronomy, and STAG Research Centre, University of Southampton, Southampton SO17 1BJ, UK

¹⁰ MIT Kavli Institute for Astrophysics and Space Research, Massachusetts Institute of Technology, Cambridge, MA 02139, USA

Received 2019 August 7; revised 2019 November 2; accepted 2019 November 4; published 2019 December 12

Abstract

Recent modeling of *Neutron Star Interior Composition Explorer* observations of thermal X-ray pulsations from the surface of the isolated millisecond pulsar PSR J0030+0451 suggests that the hot emitting regions on the pulsar's surface are far from antipodal, which is at odds with the classical assumption that the magnetic field in the pulsar magnetosphere is predominantly that of a centered dipole. Here, we review these results and examine previous attempts to constrain the magnetospheric configuration of PSR J0030+0451. To the best of our knowledge, there is in fact no direct observational evidence that PSR J0030+0451's magnetic field is a centered dipole. Developing models of physically motivated, non-canonical magnetic field configurations and the currents that they can support poses a challenging task. However, such models may have profound implications for many aspects of pulsar research, including pulsar braking, estimates of birth velocities, and interpretations of multi-wavelength magnetospheric emission.

Unified Astronomy Thesaurus concepts: Millisecond pulsars (1062); Rotation powered pulsars (1408); Neutron stars (1108)

1. Introduction

Despite 50 yr of effort and some substantial progress in the field (see the review by Beskin 2018), there is still no coherent theory of pulsar magnetospheres that would explain all of the observational data from first principles. The overwhelming majority of neutron star (NS) magnetosphere models are built upon the simplifying assumption that the large-scale external magnetic field is a centered dipole: static, retarded, and/or modified by magnetospheric currents. Quoting Gralla et al. (2017, p. 137): “This is due mainly to the high cost of numerical simulations and the lack of an obvious alternative field configuration to choose.” There is observational and theoretical evidence for higher-order multipole moments being present close to the stellar surface for the rotation-powered NSs (e.g., Jones 1980; Gil et al. 2003; Arumugasamy et al. 2018), but multipole components are assumed to be much weaker than the dipole component higher up in the magnetosphere (i.e., at larger radii). A generalization in the form of a distorted or offset dipole was also explored, both for pair production (Arons 1998; Harding & Muslimov 2011) and for the modeling of thermal pulsations from some of recycled pulsars (e.g., Bogdanov 2013).

In the canonical model of the pulsar magnetosphere, the dipole axis of the magnetic field is inclined with respect to the spin axis. The field is corotating with the star out to the radius of the light cylinder, where the corotation speed approaches the speed of light. It has been shown that highly magnetized rotating NSs cannot be surrounded by vacuum (Goldreich & Julian 1969)

and that the magnetosphere is instead filled with plasma everywhere except for narrow regions called gaps. In the gaps, the particles accelerated by the unscreened electric fields produce cascades of electron-positron pairs. These gaps are thought to be located in one (or in a combination) of the following regions: (i) near the NS surface, directly above the so-called polar caps and along the last open field line that closes within the light cylinder (where pairs are created by the strong magnetic field); and (ii) near the light cylinder and current sheet, where pairs are created by the two-photon process. The particles that stream outward are responsible for radio, γ -ray, and nonthermal X-ray emission. They also screen most of the electric field parallel to the magnetic field throughout the magnetosphere. For all gap types, the particles with the opposite charge are accelerated downward and hit the surface, heating small regions on the stellar surface and causing observable pulsed X-ray emission.

For the static inclined vacuum dipolar magnetic field configuration, the footpoints of the open magnetic field lines are located within ovals centered on the magnetic axis (hence the name “polar cap”). The vacuum-retarded dipole solution (VRD; Deutsch 1955) that takes into account the stellar rotation produces small (with respect to polar cap size) distortions and offsets in cap shape and position (Dyks & Harding 2004). However, the distorted polar caps remain antipodal.

Solutions of the global force-free (FF) pulsar magnetosphere (Contopoulos et al. 1999; Spitkovsky 2006) require specific current patterns that depend on magnetic inclination angle (Bai & Spitkovsky 2010; Timokhin & Arons 2013). These current patterns are not uniform across the polar cap; thus, hot regions

have shapes that are more complex than circles or ovals. However, the heated spots will be antipodal for a star-centered magnetic field.

As the star rotates, the heated spots generate X-ray pulsations. The shape of the pulsations (the pulse profile) as a function of photon energy depends not only on the temperature profile across the hot regions, but also on the properties of the NS atmosphere (e.g., chemical composition and ionization degree) and the gravitational field at the stellar surface. The latter makes them an invaluable tool for jointly estimating the masses and radii of NSs and thus for probing their internal composition (see Watts et al. 2016, for a review).

Recently, the *Neutron Star Interior Composition Explorer* (*NICER*; Gendreau et al. 2016) has been accruing unprecedented high-quality pulse profiles of some of the known X-ray pulsars. Riley et al. (2019, hereafter R19) performed detailed pulse-profile modeling of X-ray spectral-timing event data from *NICER* for the millisecond pulsar PSR J0030+0451.¹¹ This analysis involved relativistic ray-tracing of the thermal emission from hot regions of the pulsar’s surface and delivered joint posterior probability distributions not only for total mass and equatorial radius, but also for the thermal and geometric properties of the hot regions, and for the observer inclination to the spin axis.

The analysis of R19 suggested that the location, shape, and size of the hot regions cannot be explained with a canonical global-scale centered dipolar magnetic field configuration. In this work we review the results of R19 in the context of previous studies of PSR J0030+0451, highlighting respective caveats and limitations. We explore the implications of the results for our current understanding of pulsars and outline the prospects for future work.

2. Basic Facts about PSR J0030+0451

PSR J0030+0451 is an isolated rotation-powered millisecond pulsar (MSP). Its period of $P \approx 4.87$ ms and period time derivative of $\dot{P} \approx 1.02 \times 10^{-20} \text{ s s}^{-1}$ are typical for the known population of MSPs.¹² PSR J0030+0451 is a target in two pulsar timing array projects, the European Pulsar Timing Array (Verbiest et al. 2016) and the North American Nanohertz Observatory for Gravitational Waves (NANOGrav; Arzoumanian et al. 2018). The pulsar has been extensively observed and timed in the radio band since 2005. Its rotational and astrometric parameters (e.g., parallax and transverse proper motion) are thus relatively very well known (with respect to the overall pulsar population). Being located 329 ± 9 pc away from Earth (Arzoumanian et al. 2018), PSR J0030+0451 is one of the nearest observed MSPs. The well-constrained distance is important since it is a parameter in the pulse-profile modeling; see R19. Because of its fast rotation, PSR J0030+0451 has a relatively compact corotating magnetosphere—much smaller than the magnetospheres of non-recycled pulsars. The radius of the light cylinder, where the corotation speed is equal to the speed of light, $r_{LC} = cP/2\pi \approx 230$ km, is only a factor of 20 larger than the radius of the star itself.

Pulsed emission from PSR J0030+0451 has been detected across a wide span of frequencies, including the radio, X-ray,

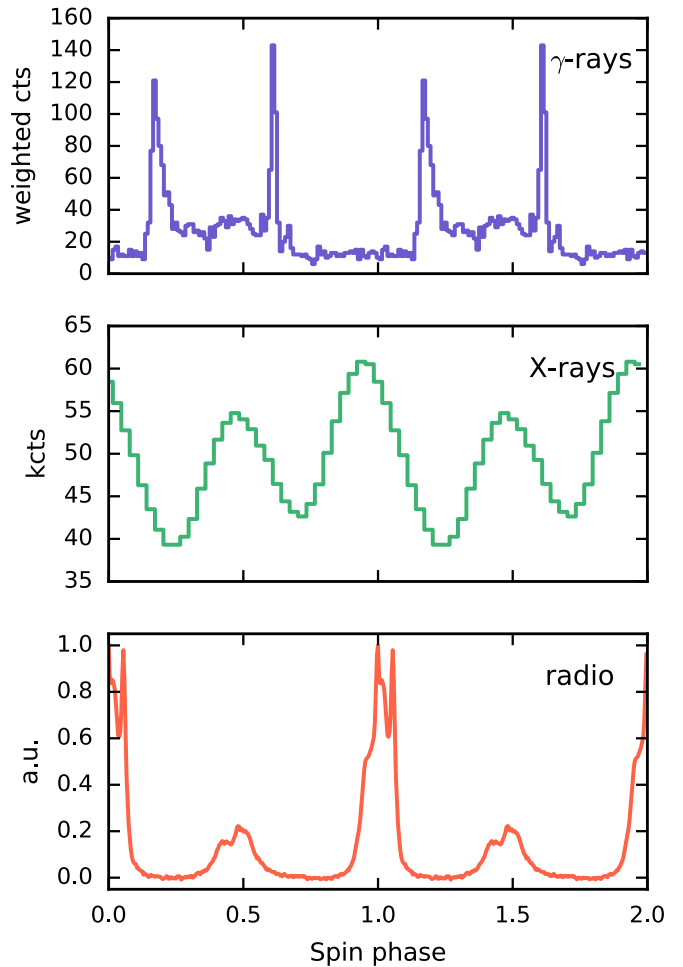


Figure 1. Average pulse profile of PSR J0030+0451’s emission in three energy bands. Top and bottom panels: γ -ray (0.1–100 GeV) and radio (1.4 GHz) profiles from the second *Fermi* pulsar catalog (Abdo et al. 2013). Middle panel: *NICER* X-ray profile (0.25–3.00 keV) from Bogdanov et al. (2019, used in R19). Radio and γ -ray profiles were produced using the same ephemerides, while an extra phase offset was added to the X-ray profile to match relative position of the X-ray profile peaks from the rigorous multi-wavelength analysis of Abdo et al. (2009).

and γ -ray bands (Figure 1). As for most MSPs, the average profile of the pulsed emission in the radio band has a rather complex shape, with two broad components separated by ~ 0.5 in spin phase (Lommen et al. 2000). Each component consists of several tightly spaced sub-components, with frequency-dependent relative peak heights. The pulsar exhibits detectable levels of linearly and circularly polarized radio emission, with the position angle of the linearly polarized radiation varying both with spin phase and observing frequency (Gentile et al. 2018). The collection of multi-wavelength properties indicates that the radio emission from PSR J0030+0451 is unlikely to be generated close to the light cylinder via caustic bunching (Espinoza et al. 2013; Johnson et al. 2014; Bilous et al. 2015).

The average profile of PSR J0030+0451’s 0.1–100 GeV γ -ray pulsations consists of two sharply peaked components with bridge emission between them. In the X-ray band, the pulse profile is composed of two broad sinusoidal peaks. Both the X-ray and radio profile components are offset from those in the γ -ray band (Abdo et al. 2009; Johnson et al. 2014).

Most rotation-powered pulsars exhibit broad pulsations with soft X-ray spectra that rapidly decline in flux above ~ 2 keV

¹¹ An independent analysis of the same data has also been carried out by Miller et al. (2019); these authors report similar hot-region geometry and properties using different models and methodology.

¹² <http://www.atnf.csiro.au/research/pulsar/psrcat>; see also Manchester et al. (2005).

(e.g., Bogdanov et al. 2006; Zavlin 2006).¹³ Previous studies using imaging observations with *XMM-Newton* have shown that the phase-averaged X-ray spectrum of PSR J0030+0451 (Bogdanov & Grindlay 2009) is best described by a model in which $\sim 95\%$ of the photons below ~ 2 keV have a thermal origin, while nonthermal radiation (such as may arise from particle acceleration in the pulsar magnetosphere), which is expected to have a power-law spectrum, cannot account for the observed spectral shape. Thus, the observational evidence strongly favors a thermal origin for the observed soft X-rays from PSR J0030+0451.

3. Geometry from Interpretation of the Multi-wavelength Profiles

Prior to R19, there were several attempts to infer the configuration of the magnetic field in PSR J0030+0451's magnetosphere using the shape of its radio and γ -ray profiles. All of these estimates relied on simplifying assumptions about the magnetic field structure, which was taken to be either a static dipole (Lommen et al. 2000; Du et al. 2010), a retarded rotating vacuum dipole (Venter et al. 2009; Johnson et al. 2014; Bezuidenhout et al. 2017), or a split monopole for the striped wind model of γ -ray emission (Pétri 2011; Chang & Zhang 2019). Under such assumptions the shape of the observed profiles is determined by two parameters: the angle α between the spin and dipolar magnetic axes; and the angle ζ between the spin axis and the line of sight (LOS).

The various approaches resulted in a variety of (α, ζ) pairs, with the general trend being toward having the magnetic pole close to the rotational equator (α close to 90°) and the LOS passing within about 10° – 20° of the magnetic pole (see the Appendix). None of the models could explain all of the features of the observed emission. In the radio band, the variation of position angle of the linearly polarized emission did not resemble that predicted by the toy rotating vector model (Lommen et al. 2000; Gentile et al. 2018; a behavior fairly common for the MSPs). Furthermore, the component width in a wide frequency range challenged the foundations of empirical radio emission height estimates that were built into joint γ -ray and radio fits (Venter et al. 2009; Johnson et al. 2014). Despite being based on emission microphysics, models of γ -ray emission do not accurately reproduce the relative peak heights of profile components and the amount of bridge emission. For further details on previous geometry estimates; see the Appendix.

The analysis presented by R19 assumed thermal emission (Section 2), but made no assumptions about the configuration of the magnetic field or the mechanism of surface heating. The observed X-ray profiles were modeled assuming two distinct hot regions on the stellar surface (motivated by the presence of two distinct pulses in the pulse profile) filled with fully ionized hydrogen atmosphere of a single local comoving effective temperature. The authors explored several models for the morphology and topology of individual hot regions, and allowed for the possibility of the heated regions being non-antipodal and non-identical. The various shapes for the hot

regions included the following: simply connected regions with circular boundaries; rings, with the *hole* both concentric and offset relative to the exterior boundary; and crescents. Model comparison in the context of the observational data led to inference of a superior hot-region configuration in terms of performance. This was achieved using a combination of measures including graphical posterior predictive checking,¹⁴ Bayesian evidence¹⁵ comparison, and likelihood function comparison (see Section 3 of R19 for details). Models comprising two circular single-temperature spots—in particular those whose spots are defined to be antipodally reflection-symmetric with respect to the stellar center—were strongly disfavored a posteriori.

The model ST-S, characterized by antipodally reflection-symmetric circular hot spots, was found to generate an X-ray signal that when combined with a background signal appears qualitatively similar to the real *NICER* data (i.e., as determined by the human eye), minus some systematic residual structure that emerges clearly as a function of phase (see the ST-S variant of figure set 13 in R19, available online). However, upon further examination of the ST-S model, it was shown that the joint spectrum generated by the hot regions far exceeds (at $E \lesssim 2$ keV) a spectral upper-bound derived from earlier analysis by Bogdanov & Grindlay (2009) of low-background *XMM-Newton* imaging observations (we refer the reader to the ST-S variant of Figure 15 in R19, available online). Moreover, the star must be both relatively massive ($M \sim 3 M_\odot$) and large ($R_{\text{eq}} \sim 16$ km) to generate a signal that even resembles the observations (see the ST-S variant of Figure 19 in R19, available online).¹⁶ If R19 had imposed stronger restrictions on the exterior spacetime solution and on the background, we can deduce that the ST-S model would have performed worse when confronted with the data. In summary, when the antipodally reflection-symmetric variant of the surface radiation field performs maximally: (i) the brightness of the source is inconsistent with observational knowledge, and (ii) the exterior spacetime is inconsistent with both observational knowledge and dense matter theory.

In response to this, R19 broke the antipodal reflection symmetry to define the ST-U model: they endowed the hot regions with distinct parameters and relaxed the prior support for the geometric configuration of those regions. This model variant far outperformed the ST-S variant, but was ultimately deemed inferior to several higher-complexity variants. Within the prior support of the ST-U variant were configurations characterized by antipodal and near-antipodal hot regions, with and without commensurate angular extents and temperatures. However, for both ST-U and the other higher-complexity models (one of which defined two temperature components per hot region, while others defined additional region shape parameters), the Bayesian evidence strongly favored both hot regions being located in the same rotational hemisphere—no matter what their shape—and separated by $\sim 90^\circ$ along a great circle connecting fiducial points (such as centers). For such configurations, neither the exterior spacetime nor the brightness of the source were anomalous when confronted with existing knowledge.

¹³ The three notable exceptions among the MSP population are the energetic PSRs J0218+4232, B1821–24, and B1937+21, which show what are unambiguously nonthermal X-ray pulsations, with very narrow pulse profiles and hard power-law spectra (with spectral photon indices of $\Gamma \approx 1$) that are also detectable in hard X-rays up to at least ~ 50 keV (see, e.g., Gotthelf & Bogdanov 2017, and references therein).

¹⁴ Whether the model is capable of generating synthetic event data a posteriori without obvious residuals in comparison with the observed data.

¹⁵ I.e., the prior predictive probability of the data conditional on a model.

¹⁶ The star would thus be reasonably compact, with $GM/R_{\text{eq}}c^2 \sim 0.27$, but this is unremarkable alone.

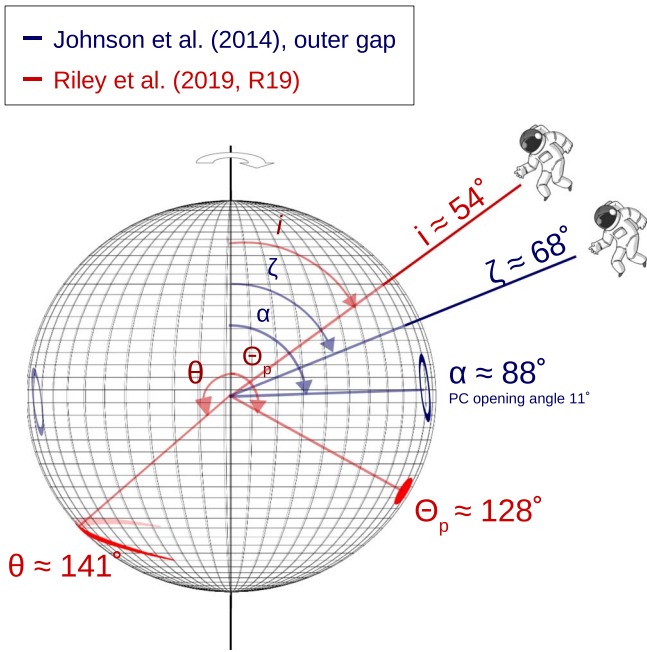


Figure 2. Cartoon showing both the magnetospheric geometry inferred from the X-ray pulsations by R19 and the geometry inferred from γ -ray/radio pulsations by Johnson et al. (2014). In the work of Johnson et al. (2014) α is the angle between the spin and dipole magnetic axes, and ζ is the angle between the spin axis and the observer’s LOS (Earth direction). For the VRD magnetic field configuration employed by Johnson et al. (2014), polar caps are antipodal. The location of the outer gaps—across which the heating may occur—are crudely rendered as blue rings, disregarding the gap thickness and small offset/shape distortions caused by rotational sweepback of the field lines. For R19, i marks the Earth inclination (denoted as ζ in Johnson et al. 2014). The colatitudes of the hot regions in R19 (shaded with red color) are marked as: Θ_p for the center of the circular hot spot; and θ for a fiducial point in the thickest segment of the hot crescent (see Figure 3). For both R19 and Johnson et al. (2014) two equatorially reflection-symmetric configurations of emission and observer are possible; here we choose the LOS to be in the northern rotational hemisphere. The longitudinal offset between the geometries of R19 and Johnson et al. (2014) is arbitrary.

In the overall superior configuration, one hot region subtended an angular extent of only a few degrees (in spherical coordinates with origin at the stellar center)—it is well approximated by a small circular spot, and on the relevant angular scales, the likelihood function is insensitive to the finer details of the shape (see R19 for detailed reasoning). For this small hot region, the 68% credible intervals for the colatitude and angular radius are approximately $\pm 6^\circ$ and $\pm 0.6^\circ$, respectively (Figure 3). The other hot region is far more azimuthally extended with respect to the pulsar spin axis and has the form of a narrow hot crescent or arc (see Figure 2). R19’s analysis is clearly sensitive to the shape of this hot region being crescent-like. For instance, the maximum fractional angular width is typically $w/\zeta_s \ll 1$, where ζ_s is the angular radius of the circular convex (or outer) boundary. Moreover, the width w is far smaller than the half-angle $\Delta\varphi$ from the symmetry line¹⁷ to a terminal point (or “horn”). This inference emerges despite ring-like and simply connected circular regions being supported a priori. Referring to Figure 3, and specifically the crescent region, the 68% credible interval widths on each of the associated spherical angles are $\mathcal{O}(10^{-2}\text{--}10^{-1})$ in units of 180° . These angles¹⁸ are: the

¹⁷ Corresponding to a great circle when projected onto, e.g., the unit sphere.

¹⁸ See also Table 2 of R19, wherein alternative parameterization is reported.

maximum crescent thickness, the crescent half-angle, and the position (defined as the colatitude of the fiducial point) and the longitudinal separation of the fiducial point from the small circular region, both with respect to the spin axis. The effective temperatures (assuming a hydrogen atmosphere) of the hot regions were tightly inferred to be $\sim 1.3 \times 10^6$ K, irrespective of their shapes.

The results obtained by R19 are, of course, conditional upon the models (including priors) assumed in the analysis. While the models considered are reasonable phenomenological representations of predictions from numerical simulations of pulsars (e.g., Harding & Muslimov 2011; Gralla et al. 2017), simplifications were made. R19 neglected, for example, the possibility of smoothly varying temperature gradients in the closed heated regions, and considered only a specific set of possible shapes for those regions.¹⁹ The prior support may also have been too broad. For instance, the two hot regions were not restricted to be near-antipodal: they were permitted to make contact, and a wide range of intermediate separations up to extreme contact-configurations may not be physically reasonable. Nonetheless it is clear that the superior configuration generates synthetic data whose residual structure in comparison to the real data is consistent with Poisson noise.

Under dipole (or modified dipole) magnetospheric field models, the hot regions—which may be of intricate shape, being set by the specifics of the particle production and acceleration—are located within the polar cap, bounded by the last open magnetic field line.²⁰ For VRD fields the shape and location of the polar cap rim departs somewhat from the oval static dipole shape; however, this departure is smaller than the size of the cap itself (Dyks & Harding 2004).

Figure 2 compares the superior configuration of hot regions from R19 with the possible hot-region locations from Johnson et al. (2014; see Appendix for the other models). The magnetospheric geometry of Johnson et al. (2014) is based on an outer gap model for γ -rays and a phenomenological model of radio emission. It also includes the quantitative fit to radio/ γ -ray profile shapes, whereas the other models use qualitative matching, radio or γ -ray information, or very simplistic radio models (see the Appendix). In the case of R19, acceleration gap physics is unspecified, meaning that the hot regions would each occupy a part of an acceleration gap whose shape is unknown. In Johnson et al. (2014), on the other hand, the assumed outline of the gap is shown, with hot regions contained therein.

As it is evident from Figure 2 and the Appendix, it is seemingly impossible to reconcile the results from R19 with a traditional centered dipolar magnetic field configuration.

4. Previous Studies of Pulsar Multipole and Offset Dipole Magnetic Fields

The shape of the hot regions (often termed “hot spots”) on the surface of NSs is in theory determined by the footpoints of the open magnetic field lines along which pair production occurs, either above the NS surface or higher up in the

¹⁹ R19 did crudely consider temperature variation in the form of hot regions with two free and distinct temperature components; a posteriori, however, this additional complexity was unhelpful to the modeling effort and was thus not pursued further in view of resource limitations.

²⁰ Another field model, the split monopole field, describes the regions of the magnetosphere beyond the light cylinder where all of the field lines are open (e.g., Bogovalov 1999). It does not offer any treatment of the polar caps.

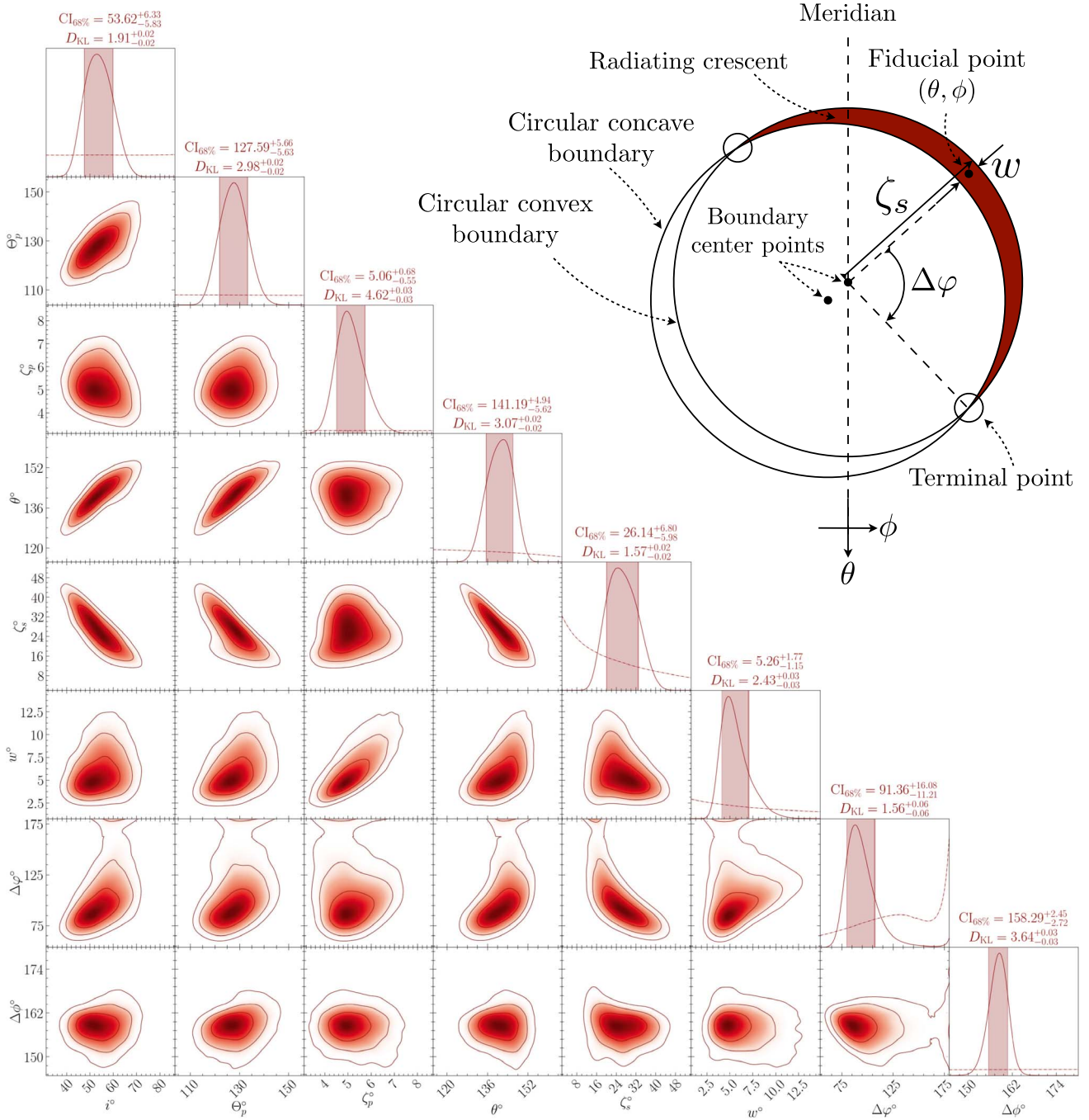


Figure 3. 1D and 2D marginal posterior density distributions for the geometric parameters (spherical angles in degrees) conditional on the R19 ST+PST model. In the top right we offer a projected schematic of the angles associated with the crescent region. The coordinates of the crescent region are defined as those of the fiducial point, midway (in angular space) between the convex and concave boundaries of the thickest segment. From left to right, the parameters are: Earth inclination i to pulsar spin axis, ST (single-temperature circular) region center colatitude Θ_p with respect to spin axis, ST region angular radius ζ_p ; PST (crescent-like) region fiducial-point colatitude θ with respect to spin axis, PST region circular convex (or outer) boundary angular radius ζ_c ; PST region maximum angular width w , the half-angle $\Delta\varphi$ of the PST region with respect to the center of the circular convex boundary, and the longitudinal separation $\Delta\phi$, with respect to the spin axis, of the center of the ST region from the fiducial point in the crescent. The azimuthal coordinate of the fiducial point is implicit in the separation $\Delta\phi$. The half-angle $\Delta\varphi$ is that subtended along the convex boundary of the crescent, from the line of symmetry to a terminal point; strictly, the prior density diverges at $\Delta\varphi = 180^\circ$ because there is prior support for regions with the topology of a ring, for which the half-angle is defined as 180° . We display the marginal prior density distributions for each parameter as the dashed-dotted functions in the on-diagonal panels. The marginal credible intervals, bounded approximately by the 16% and 84% quantiles in posterior mass, are displayed in the on-diagonal panels as the vertical red shaded bands, and given numerically by $CI_{68\%}$. The highest-density 2D credible regions containing 68%, 95%, and 99.7% of the posterior mass are also rendered in the off-diagonal panels. We give the estimated Kullback–Leibler divergences D_{KL} in bits for each parameter to summarize prior-to-posterior information gain. We refer the reader to R19 for supplementary details about this type of posterior figure.

magnetosphere, in the regions of (partially or fully) unscreened electric field. The amount of pair production depends both on the local conditions (such as local magnetic field strength) and on the strength of the electric field parallel to the magnetic

field, which is determined by the global current—which in turn depends on the pair injection rate. This makes modeling pair production a nonlinear problem. Solving it requires simultaneous solution of the pair production microphysics and the

global model of current distribution—something that is still far from being done even for the simplest possible dipole magnetic fields. However, in the case of a near-FF magnetosphere (high pair injection rates; almost completely screened electric field) the global currents are well determined and control the pair cascade microphysics.

The mechanism of particle acceleration and pair cascade production has been studied over a number of years (Ruderman & Sutherland 1975; Arons & Scharlemann 1979). The earliest simulations of pulsar pair cascades near the NS surface (Daugherty & Harding 1982) assumed a static dipole magnetic field and a current equal to the Goldreich-Julian current, $J_{\text{GJ}} = \rho_{\text{GJ}}c$, that is uniform over the polar cap (here ρ_{GJ} is the charge density required to screen the electric field, and c is the speed of light). The pair cascades in these models were steady and time-independent, but the heating was not uniform over the polar caps due to the variation in parallel electric field (Harding & Muslimov 2001).

Since the advent of global FF models, we know that the theoretical current is not J_{GJ} everywhere across the polar caps, but has a large variation that is sensitive to the inclination angle. More recent studies of polar cap pair cascades that match the global FF currents find that the cascades are time dependent and that pairs are not produced in all locations across the polar cap. Timokhin & Arons (2013) find that pair cascades take place only in regions of the polar cap where the current is super-GJ, $J > J_{\text{GJ}}$, or anti-GJ, $J < 0$, but not in regions where the current is sub-GJ, $0 < J < J_{\text{GJ}}$. Furthermore, the cascades in the super-GJ and anti-GJ (return current) have a different character: the super-GJ cascades extract electrons from the NS surface with a space-charge-limited flow (for $\vec{B} \cdot \vec{\Omega} > 0$), and the anti-GJ current regions develop a vacuum gap that breaks down by pair creation similar to the Ruderman–Sutherland gaps (Ruderman & Sutherland 1975). The return current regions therefore develop a larger parallel electric field that can cause a larger amount of surface heating from downward-flowing particles.

The studies of pulsar pair cascades have long suggested the presence of a non-dipolar magnetic field component, because the curvature of dipolar field lines and the strength of the parallel electric fields are not sufficient to produce enough pairs (and thus radio emission) for most of the pulsar population (e.g., Ruderman & Sutherland 1975; Arons & Scharlemann 1979; Arons 1998 for polar cap and Zhang et al. 2004 for outer gap). Surface multipole fields that have much smaller radii of curvature were suggested as a possible solution. The effect of global deviations from dipolar magnetic fields on polar cap pair cascades have been explored (Harding & Muslimov 2011), motivated by evidence for non-dipolar field configurations in other related astrophysical objects such as highly magnetized white dwarfs.

Offset dipole configurations were used for fitting thermal X-ray pulsation profiles of some MSPs, motivated by the fact that component peaks are separated by less than 0.5 in spin phase (e.g., Bogdanov et al. 2007; Bogdanov 2013), or in order to explain the high pulsed fraction of the thermal X-ray emission from the old non-recycled pulsar B0943+10 (Storch et al. 2014, but see Bilous 2018). Also, axially displaced or extremely offset dipole models were employed by Bogdanov (2014) to fit the X-ray pulsations from the central compact object PSR J1852+0040.

Complex magnetic field configurations on the surface of NSs, together with the evolution of the magnetic field with time, have been quite extensively studied for young NSs with high magnetic fields (e.g., magnetars, anomalous X-ray pulsars, and soft γ -ray repeaters) whose emission is believed to be powered by the magnetic field (Bransgrove et al. 2018; Gourgouliatos & Hollerbach 2018). The accretion process that leads to the formation of MSPs may also have an influence on the field structure, leading to burial of the magnetic field (Romani 1990; Melatos & Phinney 2001; Payne & Melatos 2004) or its migration together with compressed crust (Chen & Ruderman 1993; Chen et al. 1998).

5. Implications

If not crucially affected by modeling assumptions or limitations, the results of R19 provide an independent confirmation of the (previously suggested) presence of multipole field configurations in PSR J0030+0451. However, unlike previous indirect observational/modeling hints, the inferred shape of the hot regions clearly points to the global magnetic field deviating from that of a centered dipole.

One important question when considering the implications of these findings, of course, is whether PSR J0030+0451 is truly representative of the general population of MSPs. It appears to be quite generic (see Section 2 for references). Its timing behavior (P , \dot{P}) is typical of the class, as are its gamma-ray properties. It does not show any unusual single-pulse behavior, and its radio pulsations are also typical for MSPs. It does have a more obviously double-peaked X-ray pulse profile than some of the other *NICER* targets (Bogdanov et al. 2019), but its X-ray properties are otherwise quite standard.

5.1. Magnetic Field Configurations

The inclusion of multipole fields in contemporary models of pulsar magnetospheres and pair production will require further study. We should start by asking the key question: *What field configurations are physically permitted and are able to persist throughout most of a pulsar’s life?* Once the classes of possible magnetic field configurations are narrowed down, the global current distributions can be re-calculated in the FF approximation or, optimally, in a self-consistent manner involving pair cascade microphysics. A more physically realistic model of this type could then be used to generate physically meaningful surface heating fields for inference using X-ray pulse-profile data.²¹

Steps in this direction have already been taken. Under the FF assumption, Gralla et al. (2017) explored the current distribution across the polar caps for the non-dipolar magnetosphere surrounding a perfectly conducting relativistic NS. The magnetic field configuration was chosen to be axisymmetric and consisted of centered dipolar and quadrupolar terms (labeled “quadrudipolar” by the authors). They found that when the pole is dominated by the quadrupole, the polar cap has a large-scale annular shape, not a circular shape; the pole dominated by the dipole, on the other hand, exhibits a polar cap in the shape of a small circle. The authors note that in principle any shape is allowed for non-axisymmetric fields.

The work of Gralla et al. was put to practical use by Lockhart et al. (2019), who calculated the temperature distribution across

²¹ See also the discussion in R19 on interfacing numerical theory and statistical computation via efficient likelihood function implementations.

the polar caps of PSR J0437–4715 for the quadrupolar magnetic field configuration. The authors used a simple model for the heating and subsequent propagation of X-rays through the stellar atmosphere to calculate X-ray profiles. Some of the simulated profiles were deemed able to explain, at least qualitatively, the shape and location for profile components in *XMM-Newton* PSR J0437–4715 data. It would be interesting to try to construct a similar toy model for PSR J0030+0451’s hot regions, for example introducing offset to the axisymmetric quadrupolar field or breaking the axial symmetry between dipolar and quadrupolar components, as a means of rendering an annular polar cap more crescent-like.

The magnetic field of an NS is naturally supposed to evolve during its lifetime, especially during the accretion process that leads to the formation of a MSP. Therefore, it is important to expand the analysis of R19 to different classes of NS population: younger and older non-recycled pulsars, accreting NSs, and MSPs.

5.2. Pulsar Spin-down and Associated Estimates

The possibility of having large-scale non-dipolar magnetic fields has broader implications for contemporary pulsar research. Pulsar spin-down rates, for example, are set both by the low-frequency electromagnetic waves radiated by the spinning dipole magnetic field and by the pulsar wind. If large-scale non-dipolar magnetic fields are present, then \dot{P} would have a different dependence on P , which would produce a deviation of the pulsar braking indices from the value of $n = 3$ prescribed by a toy model (e.g., Pétri 2019). Also, all crude estimates of the characteristic surface magnetic fields, birth periods, and the characteristic age rely now on the assumption of a dipolar magnetic field configuration and would in turn have to be adjusted.

5.3. Gamma-Ray and Radio Emission

Given that some interpretations of multi-wavelength magnetospheric emission are based on assumptions about the global-scale magnetic field configurations, introducing multipolar (or offset-dipolar) fields may lead to rethinking of the models of magnetospheric emission. For example, with the field geometry being externally set by the X-ray data, there may be more room for refining the parameters of γ -ray generation models. While the geometry of the current sheet is not likely to be strongly affected by multipole fields, the change in the current patterns caused by such fields (Gralla et al. 2017) could affect the distribution of the high-energy emission.

Deviations of magnetic field configuration from that of a centered dipole may also be able to explain the long-known discrepancies between the observed properties of the radio emission and the properties predicted by the traditional radio emission geometries (Rankin 1993; Arzoumanian et al. 2002). This is especially so for the MSPs with their compact magnetospheres, where non-canonical field components may be relatively more prominent at the radio emission heights (Chung & Melatos 2011). The *NICER* result for PSR J0030+0451 implies that we as observers subtend—with respect to the stellar center—a sufficiently large angle to the polar caps that larger radio beam emission angles are required for visibility. We note that for proper modeling of radio pulsation profiles, the intra-magnetospheric radio propagation effects

must be also included, e.g., as described by Hakobyan et al. (2017).

5.4. Pulsar Space Velocities

Strong non-centered dipole or multipole fields can also affect estimates of pulsar space velocities. Such fields produce asymmetries in the Poynting flux of low-frequency radiation parallel to the spin axis, accelerating the pulsar by means of an electromagnetic rocket effect (Harrison & Tademaru 1975). Including the factor of four increase in the resulting accelerating force noted by Lai et al. (2001), the kick velocity is

$$V \simeq 248 \text{ km s}^{-1} \left(\frac{s}{10 \text{ km}} \right) \left(\frac{\nu_0}{10^3 \text{ Hz}} \right)^3 \frac{\mu_z \mu_\phi}{(\mu_\rho^2 + \mu_\phi^2)} \quad (1)$$

where s is the offset of the dipole from the rotation axis with cylindrical components μ_ρ , μ_ϕ , μ_z , and ν_0 is the initial spin frequency. Since MSPs are spun up to a maximum $\nu_0 \sim 1$ kHz by accretion torques (Alpar et al. 1982) and the magnetic field must be offset by a significant fraction of the stellar radius to account for both PSR J0030+0451 hot spot locations being far below the equator, the pulsar could have attained a sizeable kick velocity. However, the effect is maximal for nearly aligned rotators and the large inclination angle inferred by the γ -ray fit, implying small μ_z , would produce a smaller kick velocity. On the other hand, if millisecond pulsars have nearly aligned dipole fields following their spin-up phase due to crustal plate motions (Ruderman 1991) and then evolve to misaligned fields, the kick velocity could be higher. The above estimate is for an offset dipole; if quadrupole or higher multipole components dominate the spin-down luminosity, as could be the case for PSR J0030+0451, then the expression for the kick velocity would change. It must be noted that measuring the 3D velocity of a pulsar is difficult because the radial component of the velocity is hard to disentangle from the intrinsic second time derivative of pulsar period \ddot{P} (see the extensive discussion in Liu et al. 2018, 2019). Even for such a well-timed pulsar as PSR J0030+0451, the radial velocity is at present unknown. The velocity of solitary MSPs could also be influenced by binary disruption.

5.5. Mode-switching Pulsars

The so-called “mode-switching pulsars” may provide a very interesting test of the profile fitting scheme, and of models of multipole magnetic fields, pair cascade generation, and surface heating. These are old, non-recycled pulsars with a few stable modes of multi-wavelength emission, which includes correlated radio and thermal X-ray pulsations (e.g., a *NICER* target PSR B0943+10; Hermsen et al. 2013; Mereghetti et al. 2016, or PSR B0823+26; Hermsen et al. 2018). Mode-separated X-ray profiles can be modeled completely independently in order to test whether the estimates of shared parameters are concordant—e.g., the observer’s inclination ζ (also denoted as i in this present work), or the stellar compactness. Alternatively, the maps of the hot regions via joint estimation of key shared parameters can serve as input for models of different magnetospheric current distributions and for models of gaps within a given global magnetic field configuration (Timokhin 2010; Szary et al. 2015).

6. Conclusions

Recent modeling of *NICER* observations of the thermal X-ray pulsations generated by PSR J0030+0451 has indicated a strong preference for hot surface regions that are seemingly impossible when confronted with canon. The heating cannot be reconciled with that by magnetospheric currents at the footpoints of open field lines in canonical models of global magnetic fields—be it a centered dipole, static, or vacuum-retarded. The superior heating configuration inferred by R19 features two hot regions whose shapes are remarkably different (a spot and a larger-scale crescent) and that are located in the same rotational hemisphere.

The inferences of R19 may yet be proven to be sensitive to simplifying assumptions, for example: atmosphere chemical composition and ionization degree, the choice to neglect smooth temperature gradients across the hot regions, the consideration of a specific set of hot-region shapes (which can be too general, or, on the contrary, too specific given their phenomenological nature), and/or the background treatment. It will also be interesting to see whether similar results for the inferred properties of the hot regions are obtained for the other pulse-profile modeling sources targeted by *NICER*.

If not critically affected by the caveats, the results of R19 open a new and interesting direction in pulsar research, calling for the development of physically motivated, globally non-dipolar (or offset-dipolar) magnetic field configurations for rotation-powered pulsars, as well as including them into existing models of pair cascade production, magnetospheric current distribution, and surface heating. At the same time, more physically motivated models (including priors) for the hot-region shapes can be used to refine the models of thermal pulsations.

The existence of global non-dipolar (or offset-dipolar) magnetic field configurations may have a profound impact on many aspects of pulsar science, e.g., on pulsar braking, birth velocities, detectability, and/or the interpretation of multi-wavelength magnetospheric emission. Magnetic field configuration is naturally expected to evolve during the life of a pulsar, and it is therefore very important to predict heating distributions for a wide range of pulsars at different evolutionary stages. A sub-class of mode-switching rotation-powered pulsars may be especially interesting because their magnetosphere can be in any of several different states in a given observation epoch, and can thus exhibit different X-ray/radio emission signatures. Such emission states should differ according to the surface heating configuration and the magnetospheric current distribution, but, crucially, share the same global magnetic field configuration, observer impact angle, and stellar compactness.

This work was supported in part by NASA through the *NICER* mission and the Astrophysics Explorers Program. A.V.B., A.L.W., and T.E.R. acknowledge support from ERC Starting grant No. 639217 CSINEUTRONSTAR (PI: Watts). This work was sponsored by NWO Exact and Natural Sciences for the use of supercomputer facilities, and was carried out on the Dutch national e-infrastructure with the support of SURF Cooperative. This research has made extensive use of NASA’s Astrophysics Data System Bibliographic Services (ADS) and the arXiv.

Appendix Previous Geometry Estimates

Based on radio observations at 430 MHz, Lommen et al. (2000) attempted to match the position angle of linearly polarized radiation with a set of curves predicted by the rotating vector model with a static dipole magnetic field (RVM; Radhakrishnan & Cooke 1969). Motivated by the presence of an interpulse component in the average profile, the authors chose trial values of the inclination angle α to be either close to 0° (near-aligned case, both components coming from the ring-like emitting region above one magnetic pole) or close to 90° (orthogonal case, components coming from opposite magnetic poles). Neither near-aligned nor near-orthogonal models provided an acceptable match. It is also worth noting that the slope of the position-angle curve changes with observing frequency (Gentile et al. 2018), which is not possible in the classical rotating vector model. Several factors may be invoked to explain the poor match with the dipole magnetic field configuration: a combination of relativistic effects and radio wave propagation in the magnetosphere; improper data averaging due to the presence of orthogonal polarization modes; and the presence of polarized off-pulse emission. Currently, it is unclear whether these factors can explain the observed deviations.

After the launch of *Fermi* and the subsequent discovery of PSR J0030+0451’s γ -ray emission, several authors used the shape of the pulsar’s profiles to estimate the magnetospheric geometry. Venter et al. (2009) and Johnson et al. (2014) performed joint modeling of radio and γ -ray profiles. The authors relied on the VRD field model, with γ -ray photons originating in the gaps close to the polar cap rims (two-pole caustics (TPC) or outer gap (OG)). These geometric models assumed constant emissivity along magnetic field lines. In Venter et al. (2009), $\alpha = 70^\circ$, $\zeta = 80^\circ$ for TPC and $\alpha = 80^\circ$, $\zeta = 70^\circ$ for OG. In Johnson et al. (2014), TPC was disfavored because it did not reproduce the number of peaks in the average radio profile for any set of trial values. The OG model resulted in $\alpha = (88^{+1}_{-2})^\circ$ and $\zeta = (68 \pm 1)^\circ$.

For the radio emission, Venter et al. (2009) and Johnson et al. (2014) relied on the phenomenological recipe for radio emission height, which was earlier derived from the analysis of the multi-frequency radio profile widths of a few-dozen pulsars, not including PSR J0030+0451 (Kijak & Gil 2003). Emission heights were calculated using a geometric method based on the assumption that the radio emission on the edge of the average profile is emitted tangentially to the bundle of the last open field lines of a static dipole field. The collection of derived multi-frequency emission heights for a number of pulsars were fit on a log scale with an empirical formula involving P , \dot{P} , and observing frequency. For PSR J0030+0451’s parameters the emission height is given as $r_{\text{em}} = 3.6R_{\text{NS}} \nu_{\text{GHz}}^{-0.26}$.

Pulsed radio emission from PSR J0030+0451 has been observed at frequencies ranging from 42.1 to 1800 MHz (Pennucci 2015; Kondratiev et al. 2016). Across this frequency range, the full width of the main component at the lowest emission levels stays roughly the same, about 0.3 rotational phase cycles, although it is hard to determine it exactly given the limited signal-to-noise ratio of low-frequency radio observations. According to the empirical formula, emission heights for the observed radio emission range from 3 to $8R_{\text{NS}}$, spanning about a quarter of the light-cylinder radius. For an almost orthogonal rotator, the profile width is directly

proportional to the opening angle of the emission cone (Gil et al. 1984), which is in turn proportional to $r_{\text{em}}^{0.5}$ (Kijak & Gil 2003). Thus, between the lowest and highest frequency, the width of the main component should change by a factor of $\sqrt{3}/8 \approx 0.6$, which is seemingly not supported by the observations, unless the components at the lowest frequencies have broad wings hiding in the noise. Thus, it is unclear whether the phenomenological recipe for the radio emitting region can be applied to PSR J0030+0451 at all, given that its properties deviate from what is expected from the toy model.

Alternative locations for the γ -ray emission were explored by Du et al. (2010; annular gap, $\alpha = 35^\circ$, $\zeta = 52.6^\circ$), and by (Pétri 2011; $\alpha = 67^\circ$, $\zeta = 85^\circ$) and Chang & Zhang (2019; striped wind, $\alpha = (79_{-7}^{+12})^\circ$, $\zeta = (60_{-6}^{+10})^\circ$). In the annular gap model, γ -rays come from the vicinity of the null charge surface of the last open field lines, well below the light-cylinder radius. The striped wind model places the γ -ray emitting regions beyond the light cylinder, with γ -rays originating via inverse Compton scattering of cosmic microwave background photons by high-energy electrons. Both models make assumptions about the magnetic field configuration (dipole in case of the annular gap and split monopole for the striped wind) and the functional form of the γ -ray emissivity profile. The geometry estimates of Pétri (2011) used the radio data as well, assuming radio emission coming from the surface of the star and a Gaussian emissivity profile across the polar cap. It must be noted that in order to match the radio peaks, the author had to increase the size of the polar cap emitting region to a significant fraction of the stellar surface. The predicted radio to gamma-ray phase lag still deviated from the observed one by 0.1 cycles in phase.

Overall, no existing models of PSR J0030+0451's γ -ray emission reproduce the properties of the observed profile perfectly—e.g., the relative peak height of the components and the amount of inter-component emission.

ORCID iDs

A. V. Bilous  <https://orcid.org/0000-0002-7177-6987>
 A. L. Watts  <https://orcid.org/0000-0002-1009-2354>
 A. K. Harding  <https://orcid.org/0000-0001-6119-859X>
 T. E. Riley  <https://orcid.org/0000-0001-9313-0493>
 S. Bogdanov  <https://orcid.org/0000-0002-9870-2742>
 P. S. Ray  <https://orcid.org/0000-0002-5297-5278>
 S. Guillot  <https://orcid.org/0000-0002-6449-106X>
 W. C. G. Ho  <https://orcid.org/0000-0002-6089-6836>
 D. Chakrabarty  <https://orcid.org/0000-0001-8804-8946>

References

- Abdo, A. A., Ackermann, M., Atwood, W. B., et al. 2009, *ApJ*, 699, 1171
 Abdo, A. A., Ajello, M., Allafort, A., et al. 2013, *ApJS*, 208, 17
 Alpar, M. A., Cheng, A. F., Ruderman, M. A., & Shaham, J. 1982, *Natur*, 300, 728
 Arons, J. 1998, in Proc. International Conf. Neutron Stars and Pulsars: Thirty Years after the Discovery, ed. N. Shibasaki et al. (Tokyo: Universal Academy Press), 339
 Arons, J., & Scharlemann, E. T. 1979, *ApJ*, 231, 854
 Arumugasamy, P., Kargaltsev, O., Posselt, B., Pavlov, G. G., & Hare, J. 2018, *ApJ*, 869, 97
 Arzoumanian, Z., Brazier, A., Burke-Spolaor, S., et al. 2018, *ApJS*, 235, 37
 Arzoumanian, Z., Chernoff, D. F., & Cordes, J. M. 2002, *ApJ*, 568, 289
 Bai, X.-N., & Spitkovsky, A. 2010, *ApJ*, 715, 1282
 Beskin, V. S. 2018, *PhyU*, 61, 353
 Bezuidenhout, T., Venter, C., Seyffert, A., & Harding, A. K. 2017, in 5th Annual Conf. on High Energy Astrophysics in Southern Africa, 18
 Bilous, A. V. 2018, *A&A*, 616, A119
 Bilous, A. V., Pennucci, T. T., Demorest, P., & Ransom, S. M. 2015, *ApJ*, 803, 83
 Bogdanov, S. 2013, *ApJ*, 762, 96
 Bogdanov, S. 2014, *ApJ*, 790, 94
 Bogdanov, S., & Grindlay, J. E. 2009, *ApJ*, 703, 1557
 Bogdanov, S., Grindlay, J. E., Heinke, C. O., et al. 2006, *ApJ*, 646, 1104
 Bogdanov, S., Guillot, S., Ray, P. S., et al. 2019, *ApJL*, 887, L25
 Bogdanov, S., Rybicki, G. B., & Grindlay, J. E. 2007, *ApJ*, 670, 668
 Bogovalov, S. V. 1999, *A&A*, 349, 1017
 Bransgrove, A., Levin, Y., & Beloborodov, A. 2018, *MNRAS*, 473, 2771
 Chang, S., & Zhang, L. 2019, *MNRAS*, 483, 1796
 Chen, K., & Ruderman, M. 1993, *ApJ*, 408, 179
 Chen, K., Ruderman, M., & Zhu, T. 1998, *ApJ*, 493, 397
 Chung, C. T. Y., & Melatos, A. 2011, *MNRAS*, 415, 1703
 Contopoulos, I., Kazanas, D., & Fendt, C. 1999, *ApJ*, 511, 351
 Daugherty, J. K., & Harding, A. K. 1982, *ApJ*, 252, 337
 Deutsch, A. J. 1955, *AnAp*, 18, 1
 Du, Y. J., Qiao, G. J., Han, J. L., Lee, K. J., & Xu, R. X. 2010, *MNRAS*, 406, 2671
 Dyks, J., & Harding, A. K. 2004, *ApJ*, 614, 869
 Espinoza, C. M., Guillemot, L., Çelik, Ö, et al. 2013, *MNRAS*, 430, 571
 Gendreau, K. C., Arzoumanian, Z., Adkins, P. W., et al. 2016, *Proc. SPIE*, 9905, 99051H
 Gentile, P. A., McLaughlin, M. A., Demorest, P. B., et al. 2018, *ApJ*, 862, 47
 Gil, J., Gronkowski, P., & Rudnicki, W. 1984, *A&A*, 132, 312
 Gil, J., Melikidze, G. I., & Geppert, U. 2003, *A&A*, 407, 315
 Goldreich, P., & Julian, W. H. 1969, *ApJ*, 157, 869
 Gotthelf, E. V., & Bogdanov, S. 2017, *ApJ*, 845, 159
 Gourgouliatos, K. N., & Hollerbach, R. 2018, *ApJ*, 852, 21
 Gralla, S. E., Lupsasca, A., & Philippov, A. 2017, *ApJ*, 851, 137
 Hakobyan, H. L., Beskin, V. S., & Philippov, A. A. 2017, *MNRAS*, 469, 2704
 Harding, A. K., & Muslimov, A. G. 2001, *ApJ*, 556, 987
 Harding, A. K., & Muslimov, A. G. 2011, *ApJL*, 726, L10
 Harrison, E. R., & Tademaru, E. 1975, *ApJ*, 201, 447
 Hermsen, W., Hessels, J. W. T., Kuiper, L., et al. 2013, *Sci*, 339, 436
 Hermsen, W., Kuiper, L., Basu, R., et al. 2018, *MNRAS*, 480, 3655
 Johnson, T. J., Venter, C., Harding, A. K., et al. 2014, *ApJS*, 213, 6
 Jones, P. B. 1980, *MNRAS*, 192, 847
 Kijak, J., & Gil, J. 2003, *A&A*, 397, 969
 Kondratiev, V. I., Verbiest, J. P. W., Hessels, J. W. T., et al. 2016, *A&A*, 585, A128
 Lai, D., Chernoff, D. F., & Cordes, J. M. 2001, *ApJ*, 549, 1111
 Liu, X. J., Bassa, C. G., & Stappers, B. W. 2018, *MNRAS*, 478, 2359
 Liu, X. J., Keith, M. J., Bassa, C. G., & Stappers, B. W. 2019, *MNRAS*, 488, 2190
 Lockhart, W., Gralla, S. E., Özel, F., & Psaltis, D. 2019, *MNRAS*, 490, 1774
 Lommen, A. N., Zepka, A., Backer, D. C., et al. 2000, *ApJ*, 545, 1007
 Manchester, R. N., Hobbs, G. B., Teoh, A., & Hobbs, M. 2005, *AJ*, 129, 1993
 Melatos, A., & Phinney, E. S. 2001, *PASA*, 18, 421
 Mereghetti, S., Kuiper, L., Tiengo, A., et al. 2016, *ApJ*, 831, 21
 Miller, M. C., Lamb, F. K., Dittmann, A. J., et al. 2019, *ApJL*, 887, L24
 Payne, D. J. B., & Melatos, A. 2004, *MNRAS*, 351, 569
 Pennucci, T. T. 2015, PhD thesis, Univ. Virginia
 Pétri, J. 2011, *MNRAS*, 412, 1870
 Pétri, J. 2019, *MNRAS*, 485, 4573
 Radhakrishnan, V., & Cooke, D. J. 1969, *ApL*, 3, 225
 Rankin, J. M. 1993, *ApJ*, 405, 285
 Riley, T. E., Watts, A. L., Bogdanov, S., et al. 2019, *ApJL*, 887, L21
 Romani, R. W. 1990, *Natur*, 347, 741
 Ruderman, M. 1991, *ApJ*, 366, 261
 Ruderman, M. A., & Sutherland, P. G. 1975, *ApJ*, 196, 51
 Spitkovsky, A. 2006, *ApJL*, 648, L51
 Storch, N. I., Ho, W. C. G., Lai, D., Bogdanov, S., & Heinke, C. O. 2014, *ApJL*, 789, L27
 Szary, A., Melikidze, G. I., & Gil, J. 2015, *MNRAS*, 447, 2295
 Timokhin, A. N. 2010, *MNRAS*, 408, L41
 Timokhin, A. N., & Arons, J. 2013, *MNRAS*, 429, 20
 Venter, C., Harding, A. K., & Guillemot, L. 2009, *ApJ*, 707, 800
 Verbiest, J. P. W., Lentati, L., Hobbs, G., et al. 2016, *MNRAS*, 458, 1267
 Watts, A. L., Andersson, N., Chakrabarty, D., et al. 2016, *RvMP*, 88, 021001
 Zavlin, V. E. 2006, *ApJ*, 638, 951
 Zhang, L., Cheng, K. S., Jiang, Z. J., & Leung, P. 2004, *ApJ*, 604, 317